Advanced Materials

Additive Manufacturing and Performance of Architectured Cement-based Materials

--Manuscript Draft--

Manuscript Number:	
Full Title:	Additive Manufacturing and Performance of Architectured Cement-based Materials
Article Type:	Communication
Section/Category:	
Keywords:	direct ink writing, architectured material, hardened cement paste, interface, mechanical response, bioinspired materials
Corresponding Author:	Pablo Zavattieri Purdue University West lafayette, IN UNITED STATES
Additional Information:	
Question	**Response**
Please submit a plain text version of your cover letter here. **If you are submitting a revision of your manuscript, please do not overwrite your original cover letter. There is an opportunity for you to provide your responses to the reviewers later; please do not add them here**.	Dear Dr. Lenders, We wish to submit the paper entitled “Additive Manufacturing and Performance of Architectured Cement-based Materials” for publication in the Advanced Materials. There is a quest to use additive manufacturing for 3D printing cementitious materials. However, due to the intrinsic limited strength, brittle behavior and presence of weak interfaces, this is a very challenging task. In this article, we examine the use of bioinspired architectures to create 3D printing cementitious materials with improved mechanical properties. In our work, we demonstrate that using bioinspired architectures with clever mechanisms that prevent catastrophic failure, we are able to increase the fracture energy by more than 150% with respect to its base material without sacrificing the strength of the base materials (similar to what we also find in natural materials). We believe that this article fits into the scope of Advanced Materials as it brings important information about the role of architecture in materials. It shows controlled spread of damage through relatively weak interfaces, which is counter-intuitive in brittle materials. It also brings new insights into materials design. This is important considering that several current research efforts are actually trying to eliminate these interfaces. Please do not hesitate to contact me should you have any questions. Sincerely, Pablo Zavattieri Purdue University
Do you or any of your co-authors have a conflict of interest to declare?	No. The authors declare no conflict of interest.
Corresponding Author Secondary Information:	
Corresponding Author's Institution:	Purdue University
Corresponding Author's Secondary Institution:	
First Author:	Mohamadreza Moini
First Author Secondary Information:	
Order of Authors:	Mohamadreza Moini
	Jan Olek, PhD
	Jeffrey Youngblood, PhD
	Bryan Magee, PhD

	Pablo Zavattieri
Order of Authors Secondary Information:	
Abstract:	There is an increasing interest in Additive Manufacturing (AM) applied to cement-based materials. However, the intrinsic brittle behavior of these materials and the presence of interfaces from the additive manufacturing process represent the current major challenges. Contrary to what most research groups are doing to eliminate interfaces and add reinforcement, our work focuses on harnessing the role of relatively weak interfaces by employing clever design guidelines from bio-inspired architectured materials. These architectures play a significant role in enabling novel performance characteristics, such as toughening, spread of damage and flaw-tolerance. The control of the architecture of cement paste materials through AM allows initiation and propagation of micro-cracking at key locations in the layered structures, and can play a role in tuning, enhancing and diversifying the mechanisms that improve work of fracture, strength, and inelastic deflection of the structure. Evidence is provided by multiaxial flexural tests comparing the architectured materials with cast specimens. We observe that these architectures can significantly departure from the typical strength-porosity relationship, classically known for brittle materials. In turns, these architectures show improvements of the work of fracture by more than 150% exhibiting controlled spread of damage without sacrificing strength.

WILEY-VCH

DOI: 10.1002/((please add manuscript number))
Article type: Communication

Additive Manufacturing and Performance of Architectured Cement-based Materials

*Mohamadreza Moini, Jan Olek, Jeffrey Youngblood, Bryan Magee, Pablo D. Zavattieri**

M. Moini, Prof. J. Olek, Prof. P. D. Zavattieri

Lyles School of Civil Engineering, Purdue University at West Lafayette, Indiana 47907, USA

E-mail: zavattie@purdue.edu

Prof. J. Youngblood

School of Materials Engineering, Purdue University at West Lafayette, Indiana 47907, USA

Dr. Bryan Magee

Built Environment Research Institute, Ulster University at Newtownabbey, BT37 0QB, UK

Keywords: direct ink writing, architectured material, hardened cement paste, interface, mechanical response

Abstract:

There is an increasing interest in Additive Manufacturing (AM) applied to cement-based materials. However, the intrinsic brittle behavior of these materials and the presence of interfaces from the additive manufacturing process represent the current major challenges. Contrary to what most research groups are doing to eliminate interfaces and add reinforcement, our work focuses on harnessing the role of relatively weak interfaces by employing clever design guidelines from bio-inspired architectured materials. These architectures play a significant role in enabling novel performance characteristics, such as toughening, spread of damage and flaw-tolerance. The control of the architecture of cement paste materials through AM allows initiation and propagation of micro-cracking at key locations in the layered structures, and can play a role in tuning, enhancing and diversifying the mechanisms that improve work of fracture, strength, and inelastic deflection of the structure. Evidence is provided by multiaxial flexural tests comparing the architectured materials with cast specimens. We observe that these architectures can significantly departure from the typical strength-porosity relationship, classically known for brittle materials. In turns, these architectures show improvements of the work of fracture by more than 150% exhibiting controlled spread of damage without sacrificing strength.

There is a rising interest in hierarchical design and additive manufacturing (AM) of architectured materials due to their ability to achieve unique and novel performance characteristics [1-8]. The AM allows for fabrication of complex solid and cellular structures, and thus enables numerous opportunities for generation of novel, and unconventional behaviors via controlled mechanical responses, or enhanced properties [9-12].

The focus of this work is on 3D printing of brittle cement-based materials, in which the ability to control the internal architecture of the structure at the macroscopic (i.e. mm scale) may play a significant role by enabling novel performance characteristics, such as a quasi-brittle mechanical behavior, fracture and damage tolerance, unique load-displacement response, and enhanced flexural strength. The control of the architecture of materials through AM alters the crack propagation at the interface in layered bioinspired structures, and can play a role in tuning, enhancing and diversifying the mechanical response and toughening mechanisms [13-19]. Materials with such enhanced properties may impact design approaches, processes, and products in several industries [20,21].

Despite recent works on processing [22-24] and mechanical properties of 3D printed cement-based materials [25-30], as well as earlier works on microstructural aspects of fracture properties of cast cement paste [31-33], there are only limited studies that highlight control of the mechanical behavior through the architecture of cement-based materials [34,35]. Because the presence of weak interface is considered detrimental for the overall mechanical performance of cementitious materials, current research efforts focus mostly on eliminating or strengthening AM-induced interfaces as a mean to minimize their effect on the overall

strength, bearing capacity and improve stress transfer across or the interfaces in certain direction in 3D printed elements [26-30]. Contrary to that line of research, our work attempts to harness these relatively weak interfaces by examining the role of the architecture as a mean of controlling and diversifying the mechanical response of brittle cement paste elements.

Due to its intrinsic properties, the cast hardened cement paste (hcp) does not exhibit typical toughening mechanisms, e.g. crack branching, observed in other materials [36,37]. Correspondingly, cast cement paste behaves as brittle material and does not show non-linear behavior [38]. However, existing studies demonstrated that directionality of response, as enabled by controlling the internal architecture of the elements, can play a part in spreading of the damage, and may improve overall inelastic response of composite materials, specifically brittle ceramics and compliant organics [13-18]. In this work, the mechanical response of 3D printed cement paste elements with specific architectures, along with the associated damage mechanisms, have been investigated by examining the behavior of both, the individual filaments (i.e. layered deposited material) and the interfaces between the filaments.

Many of the internal architectures, that can be fabricated via 3D printing are not attainable, or are extremely challenging to achieve, using conventional casting methods. To illustrate this point, we present several elements with variable architectures achieved by 3D-printing of the ordinary portland cement paste using the direct-ink-writing (DIW) method. These architectures included: a closed cell honeycomb pattern (**Figure 1**a), a 'Bouligand' architecture with helicoidal alignment of filaments at pitch angles $\gamma = 2^{o}$ and 45^{o}, (**Figures**

1b,c), a grid architecture (**Figure 1**d), a cellular sandwich panel prism with solid top and bottom layers (**Figure 1**e), and a compliant structure with honeycomb pattern (**Figure 1**f).

When subjected to cycling loading, a compliant structure with honeycomb pattern (similar to that illustrated in **Figure 1**f) displayed bi-linear stress-strain behavior characterized by two discrete values of moduli of elasticity (see Figure S1 in supporting materials).

The values of modulus of rupture (MOR) of printed solid prisms with various filament orientations (i.e., 0^o, 45^o, and 90^o with respect to X-axis) were determined using the three-point-bending (3PB) test (**Figure 2**a). A comparison of average values of specific MOR for printed and cast specimens (**Figure 2**c) reveals that they were not statistically different (i.e., $p>=0.05$ for all printing angles versus cast). This implies that the mechanical response of all three of the printed prisms was independent of the orientation of the filament and the specimen processing method (i.e. printed vs. cast). Since there has been observable difference in the crack patterns as function of filament orientation (**Figure 2**d-m), the lack of statistically discernible difference in the values of specific MOR (in spite of the trends in strength between printed and cast specimen in **Figure 3**c) may simply imply that the 3PB test is not capable to adequately capture the microscopic level fracture response.

Previous research, indicated that 3D-printed cement-based elements exhibited zones of weakness at the interfaces between individual filaments [26-30], a phenomenon not commonly observed in conventionally cast prisms. The influence of pronounced interfaces on the overall crack path, and on the associated micro-cracking, has been observed to be unique for each of the 0^o and 45^o architectures used in this study. Specifically, the crack path in two types of the

tested prisms (i.e. those with 0^o and 45^o) intercepted the filaments (**Figures 2**d,e) whereas the crack path was parallel to the filament in the third type of the prism (i.e. the one with 90^o architecture). When the first two types of prisms (i.e. 0^o and 45^o) were examined in XZ plane microscopically, the crack path was observed to partially deflected to a potentially weak interface along the layered filaments (parallel to the X direction), resulting in a staggered crack pattern (**Figures 2**g,h). Furthermore, examination of **Figure 2**j,k, reveals that at the locations where the crack is being deflected along the filament (i.e. in the X-direction) there is an accompanying development of micro-cracking that spreads along the interface between the two filament. In contrast, for the prisms with 90^o orientation, only a single, predominantly unidirectional crack is developed along one of the interfaces (**Figure 2**i). Additionally, no micro-cracking was observed.

For 90^o prisms, we can infer that the overall crack localized at the interface with no crack deflection and micro-cracking advancing into the interface (**Figures 2**f,i,m). Overall, examination of the crack paths in these three architectures indicates a potential weak interface in 3D printed elements. The demonstrated crack paths in all three architectures suggest that controlling the architecture of solid prism (via varying filament orientation) can be used to control the crack path in solid 3D printed prisms. The micro-cracking at the point of crack deflection indicates that the interface can be utilized to introduce a mechanism for micro-crack propagation solid structures and allow for a new damage behavior uncommon in cast elements.

The Bouligand architectures utilized here have found applications in engineering materials and offer increased toughness and energy absorption by enabling crack propagation in a stepwise pattern, crack redirection, branching, and prevention of catastrophic failure in various biological organisms [39,40]. Moreover, previous investigations have shown that Bouligand architectures, such as those found in the endocuticles of arthropods, tend to grow cracks in twisted patterns following the direction of the fiber [39]. These twisting patterns have been found to be responsible for increasing toughness [41] and promote spread of damage [48]. To further investigate the architecture-performance relationship, Bouligand architectures printed with several pitch angles (γ = 8°, 15°, 30°, 45°, 90°) and infill percentage (60% to 100%) are studied for specific strength, and work of fracture (WOF), and load-displacement behavior, and compared with conventionally cast structures (**Figure 3**a). The Bouligand architecture demonstrated consistently higher degrees of deflection compared to cast structures. This additional degree of deflection is uncommon in brittle materials and is reflected in **Figure 3**a by 105%, 125%, and 150% for architectures with γ = 8° (60% infill), γ = 45° (60% infill), and γ = 8° (solid), respectively. It must be noted that these cellular and solid structures have achieved higher deflection while having relative densities (i.e. density of each specimen relative to the average of the conventional cast solid controls) lower than cast specimens (as low as 0.5).

As discussed in prism study above, the deflection of the crack path into the interface and presence of micro-cracks in the interfaces is also of particular importance for the printed disc structures. These two features in the Bouligand architectures can enable the spread of the

damage in the structure by localization of micro-cracks and fracture of sacrificial links without sacrificing the integrity of the structure. The damage and fracture of filaments at pre- and post-peak is additionally captured. The screen shot of the acoustic recording of the fracture during testing for $\gamma = 45^{o}$ and cast control is also illustrated in **Figure 3**a. The screen shot of the acoustic recordings qualitatively describe the propagation of multiple cracks prior- and post-peak in the Bouligand structure is distinguished when compared to fracture of cast cement in a brittle manner (**Figure 3**a). The major peaks of the acoustic graph match the local maximum loads.

In terms of specific properties, the majority of Bouligand structures (γ = 15^{o}, 30^{o}, 45^{o}, 90^{o}), other than $\gamma = 8^{o}$ with 60% infill, are statistically similar in average specific MOR when compared to cast structures (**Figure 3**b). This equivalent performance includes small pitch angle with $\gamma = 8^{o}$ with 100% infill (i.e., solid).

The WOF is assessed for all Bouligand architectures, and an increase in WOF is observed as γ increased from 8^{o} to 90^{o} for 60% infill structures (**Figure 3**c), with highest WOF in $\gamma = 90^{o}$. The observed pattern is consistent with previous studies on composite materials with the Bouligand structure, suggesting increased WOF with increase in rotation angle [33]. **Figure 3**c describes how γ or infill percentage can play a role in the fracture properties of materials. The solid structures with γ = 8^{o}, however, demonstrated elevated WOF compared to its identical γ at lower density (60% infill). This is in accordance with what is observed in similar Bouligand structures in relation to pitch angle [40]. The solid structures with $\gamma = 8^{o}$ show a counter-clock-wise orientation of the fractured plane following the right-hand pattern in

consecutive layers (positive counter-clock-wise γ). This Bouligand study demonstrates the ability to control the WOF by controlling the pitch angle and relative density in brittle materials.

The performance of Bouligand structures in terms of MOR with respect to their relative density is assessed for various γ and compared to conventionally cast 'cellular solid' over a broad range of porosity (**Figure 3**d). Apparent from **Figure 3**d, and benchmarked against theoretical curve and values of MOR for hardened cast cellular cement paste [43], is the emergence of a distinct group of printed Bouligand architectures with γ = 15-90^o (shown as a blue region in **Figure 3**d) that consistently out-performs conventionally cast specimens across the relative density range considered (0.5-0.65). This presents clear indication that higher performance is attainable by 3D printed Bouligand architectures relative to conventionally cast controls with equivalent density, reflecting the unique ability of specimen architecture to control mechanical response. Conversely, less favourable performance in terms of MOR was noted for the 60% infill, γ = 8^o specimens (**Figures 3**d).

Bouligand architectures are further studied for identification of fracture patterns, crack-paths, and micro-cracks using optical microscopy (**Figure 4**). A variety of fracture paths and crack patterns are exhibited at the bottoms (**Figures 4**a.1-c.1) and cross-sections of Bouligand architectures (**Figures 4**a.2-c.2). In γ = 45^o with 60% infill, the crack path appear to shear the filaments (**Figure 4**a.1), whereas it occurred at the interface between adjacent filaments in 8^o with 60% infill and in solid structure with 100% infill (**Figures 4**a.2,a.3). The crack path, for the γ = 45^o, typical in Bouligand structures resulted in shear failure in filaments with a certain

orientation, whereas the filaments in the layers parallel to the main failure plain remained intact (in layer 1- bottom and layer 5, **Figures 4**c.3). In contrast, with **Figures 4**c.3, horizontal propagation of crack paths at the interface is also observed at $\gamma = 8^o$ structures with 60% infill (layer 4 and 5) as demonstrated in **Figures 4**b.3,b.4. In the solid structures with $\gamma = 8^o$, the crack propagates at the interface between layers 6 and 7 throughout the cross-section and between layers 2 and 3 near the crack divergence points (**Figure 4**a.3). In addition, a staggered fractured pattern is observed in the main failure plane (**Figure 4**a.8).

Advancement of the micro-crack at the interface in solid $\gamma = 8^o$ category is further observed with multiple parallel micro-cracking throughout the cross section **(Figure 4**a.3) and at the bottom and top layer (**Figures 4**a.4,a.5,a.6). The higher WOF for solid structures with $\gamma = 8^o$ seemed higher than that for structures with 60% infill and $\gamma = 8^o$ and 45^o, and the conventionally cast discs (**Figure 3**c), may be attributed to the allowance of micro-crack advancement at the interface and may allow for the higher deflection at failure as discussed previously (**Figure 3**a).

Micro-cracking in different arrangements and in bridging elements between the filaments in Bouligand architectures are also recognized in $\gamma = 30^o$ structures. Multiple parallel micro-cracks near the fractured face of specimens at the bottom layers 1, 2 and 3 is observed (**Figures 4**d.1,d.2). These parallel micro-cracks are spaced equally from the fracture edge in the very bottom layer (**Figure 4**d.1) and appear twisting in the subsequent bottom layers 2 and 3 and at the bridging link (**Figure 4**d.2). These patterns are consistent with what was found in other in similar biomimetic Bouligand composite materials [42].

A similar sinusoidal fractured pattern is observed in both categories of Bouligand architectures, the 8º with 60% infill and solid 100% infill (**Figures 4**a.7,b.5). This pattern is repeated in solid 8º specimens between layers 6 and 7 and between layers 2 and 3 and is viewed in cross section (**Figure 4**a.3), whereas it is observed throughout the elevation view of 8º with 60% infill (**Figure 4**b.5). In the former, it is noteworthy that there is an intra-layer sinusoidal pattern between consecutive layers due to small γ (8º) and a subsequent pattern offset associated with the small angle orientation (**Figure 4**a.7), and in the later it is noteworthy that the micro-crack advancement is observed in the interface similar to other categories (**Figure 4**b.6).

Overall, in Bouligand architectures, the crack deflection at the interface is commonly observed in smaller categories of γ (8º with 60% infill and 100% solid, **Figures 4**b.3,b.4,a.1). The micro-crack advancement at the interface is also observed in various architectures (**Figures 5**a.3-a.6,b.5) indicating weaker properties at the interface. The presence of this weak interface, not only allows to control the crack path to follow the interface, but also can initiate numerous micro-crack advancement. Acknowledging this possibility, various architectures can then be tailored for the anticipated crack at the interface to follow a desirable pattern, and may provide an increased threshold to crack initiation, initiation toughness, and WOF (**Figure 3**c).

The fracture behavior of cast cement, commonly exhibits brittle and unstable crack propagation [30]. Overall, in 0º and 45º architectures in solid prism, horizontal deflection of crack is demonstrated and redirected at the interface, followed by advancement of micro-

cracks at the interface between filaments (**Figures 2**g,h). This crack deflection and the subsequent micro-crack induction, suggests the possibility of increased spread of the damage in design of these architectured materials. In 90^{o} prisms, no micro-crack or crack deflection at the interface is observed. However, a remarkable observation in this case is that the main crack occurs at the interface between the filaments in the mid-span of the specimen in the entire cross section (**Figures 3**h). This indicates the presence of interface with specific interfacial strength, distinguished from intra-filament in 3D printed prisms. The demonstrated interface between layers can be utilized in an architecture in which micro-cracks can be advanced in multi-layers and allow for an intrinsic fracture toughening mechanism [13,14].

More broadly, in both types of solid prisms and Bouligand architectures studied in this work, micro-crack advancement along the interface is observed. In most cases, the initiated micro-cracks in solid prisms (**Figure 2**g,h) and solid Bouligand structures (**Figures 4**a.3-a.6) spread all the way to the edge of the prism and disc. Moreover, these interfacial micro-cracks are straight on a macroscopic scale, and follow the architectural pattern of the interfaces, both in prism (**Figures 2**g,h) and Bouligand architectures Typical fracture features of brittle cement initiated from Knoop dent, for example, is discussed to have a macroscopic scale (merely 0.5 to 5 mm for a 3-kg indentation load) and extend straight along the dent, followed by forward and backward crack branches on the order of 10s of microns and a common termination in a short fork form [36]. In contrast, we demonstrate that the properties of the interface between the filaments can be designed to act as a crack trap leading to prompt multiple site nucleation across filaments, and eventually define the overall response of the materials in 3D printed architectures under loading.

The periodic crack patterns found in bridging elements near the failure plain in the 30^o Bouligand architecture signifies that architecture of a material can allow for induction of cracks through sacrificial links without compromising the integrity of the structure. The failure of sacrificial links does not necessarily decrease the strength (**Figure 3**b), however it can contribute to the spread the damage due to improved initiation toughness [14]. Such architectures, in spite of the brittle nature of their base materials, can undertake localized damage triggered by sacrificial links (**Figures 4**d.1,d.2) and yet be able to tolerate micro-cracks in each link. These micro-cracks can contribute to overall inelastic deformation and toughening of the material without abrupt macroscopic failure of the structure. Further understanding of such systems, can result in design of flaw-tolerant brittle architectured materials such as hardened cement paste. Practically, the growth of the micro-cracks throughout the structure avoids the localization of micro-cracks and allows multiple micro-crack propagation at the interface such as those observed in prisms and Bouligand architectures.

In summary, this work presents the role of the architecture of the materials by exploring bio-inspired design and heterogeneities induced by the interfaces as a mean of controlling and diversifying the mechanical response of brittle cement paste elements. we have demonstrated that architecture of the structure can uncover novel behaviors of cementitious materials via DIW process. These behaviors, observed in compliant design (see supporting information), prism and Bouligand architectures, demonstrate new capacities to engineering performance of cementitious materials. Architectures such as compliant design demonstrated bilinear stress-strain behavior, not attainable in cast elements, and provides the ability to customize stress-

strain behavior as applicable. In prism type structures, using architecture to control the crack path and allow advancement of multi micro-cracking (and spread of the damage) using an intrinsic fracture toughening mechanism is conceivable. Processing-induced weak interfaces are commonly considered defects in cementitious materials and are avoided. In Bouligand architectures, we demonstrated that such heterogeneities interfaces exist and are not necessarily detrimental to the overall performance, but also can provide mechanisms that can lead to novel responses such as an increased deflection in load-displacement, increased WOF, and other properties unimagined for hardened cement paste materials. In addition, the viability of deflecting the crack path at the interface and initiating micro-cracks through the interface, offers new possibilities in spread and control of the damage, in fracture mechanisms, and in hierarchical design of materials. To further explore opportunities provided by architectured cement paste materials, a fundamental understanding on the intertwined relationships between processing-induced heterogeneities, ink properties (cement hydration, rheology, chemistry, and formulation), architectural parameters (such as pitch angle and infill percentage), and microstructural characteristics of the intra-filaments and inter-filaments (interfaces) must be developed to fine tune the performance of resulting elements. Further understanding of the architectural parameters, can result in design of flaw-tolerant architectured materials with brittle base such as hardened cement paste.

Experimental Section:

Cementitious Ink Formulation: An iterative trial and error ink design procedure is used to identify cement inks suitable for DIW process. The ink with proper flow properties that can

overcome processing challenges such as flocculation, bleeding, and can result in suitable shape holding is designed. The final ink used constituted the sub 150 µm fraction of commercially available Type I cement (Buzzi Unicem USA) in accordance with ASTM C150 [44], deionized water, and both high range water reducing admixture (HRWRA-MasterGlenium 7700) and viscosity modifying admixtures (VMA-MasterMatrix 362) in accordance with ASTM C494 [45] and the findings of previous study [46]. For each 250 g of cement, the mix comprised 65.2, 1.1 and 3 g of deionized water, HRWRA and VMA, respectively.

Mixing Procedure: A Twister Evolution Venturi vacuum mixer is used in three steps to mix and eliminate entrapped air. Admixtures are added and dispersed in water and mixed with cement at 400 rpm for 25 s, at 400 rpm for 90 seconds at 70% vacuum and then finally at 400rpm at 100% vacuum.

3D Printing: A bespoke system is developed by merging a 3D printer typically used for printing thermoplastics (Ultimaker 2 Extended+) with a stepper motor-driven extrusion system (Structur3d Discov3ry Paste Extruder) capable of applying desirable extrusion rates to mounted 75 mL ink-charged syringes. The 3D printer hardware is modified by mounting a lightweight aluminium nozzle holder on the gantry for nozzle placement. The printer and extrusion system are merged through standard luer locks and polyethylene tubing. A nozzle with an internal diameter of 1.36 mm is used. Slicer-generated g-code command included X,Y, Z point cloud coordinates and E (extrusion), and F (printing speed) axis movement commands specific to each design. A 1 mm layer height and 250 mm/min printing speed is used

throughout. Specimens are transferred to a curing chamber with relative humidity of 93.58 ± 0.66 % (using potassium nitrate) at 25 °C immediately after printing or casting.

Characterization: Flexural strength and modulus-of-rupture (MOR), is used to characterize the mechanical properties via uniaxial three-point bending (3PB) testing of prism specimens and multi-axial ball-on-three-ball (B3B) testing of disc-shaped specimens. For 3PB testing, prisms are designed to have final dimensions of 12 x 12 x 40 mm, with surfaces being ground flat prior to testing to ensure acceptable tolerances and good contact with test support plates [47]. MOR is calculated based on the measured dimensions of each specimen. B3B testing is adopted given its high sensitivity to internal defects and insensitivity to outer and surface imperfections [48,49]. A load is applied via a central ball on the top face of round, disc-shaped specimen of 55 mm diameter and 8 mm thickness supported underneath by three equally sized, equidistantly spaced balls placed on a circle of diameter of 50 mm [50]. Bouligand structure discs are aligned to ensure that bottom filament orientation is aligned with the minimum stress field. A stereo microphone device (Zoom iQ6) with customizable stereo width is used to capture crack noise.

Force and displacement for both tests are measured using a 10 kN capacity test rig (MTS insight 10). All reported data is an average of at least two specimen results. Specimen relative density is calculated from measured mass and volume of each specimen divided by the average mass of conventionally cast ‘solid’ specimens. Specific MOR is calculated by dividing the MOR value for each specimen by its relative density. WOF is calculated by integrating areas under load-displacement curves. Two theoretical relationships between

porosity and strength for brittle materials are presented in **Figure 4**d and describe the strength-porosity relationship of lightweight cellular structures based on strength of a control specimen with zero porosity [43,51,52]. All specimens are tested at the age of 3 days (72±2 hours). Aluminium powder and variations of water/cement ratios are used to cast lightweight cellular specimens.

Supporting Information

Supporting Information is available from the Wiley Online Library or from the author.

Acknowledgements

The authors gratefully acknowledge generous support from the National Science Foundation (CMMI 1562927) of this research. The authors would also like to thank the BASF chemicals company for providing materials.

References

[1] U. G. Wegst, H. Bai, E. Saiz, A.P. Tomsia, R. O. Ritchie, Nat. Mater. **2015**, *14*, 23.

[2] E. B. Duoss, T.H. Weisgraber, K. Hearon, C. Zhu, W. Small, T.R. Metz, J.J. Vericella, H. D. Barth, J.D. Kuntz, R. S. Maxwell, C.M. Spadaccini, Adv. Funct. Mater. **2014**, *24*, 4905.

[3] J. P. Lewicki, J. N. Rodriguez, C. Zhu, M.A. Worsley, A.S. Wu, Y. Kanarska, J.D. Horn, E. B. Duoss, J. M. Ortega, W. Elmer, R. Hensleigh, **2017**, Sci. Rep. *7*, 43401.

[4] B. G. Compton, J. A. Lewis, Adv. Mater. **2014**, *26*, 5930.

[5] K. T. Sullivan, C. Zhu, E. B. Duoss, A. E. Gash, D. B. Kolesky, J. D. Kuntz, J.A. Lewis, C.M. Spadaccini, Adv. Mater. **2016**, *28*, 1934.

[6] A.S. Gladman, E.A. Matsumoto, R. G. Nuzzo, L. Mahadevan, J. A. Lewis, Nat. Mater. **2016**, *15*, 413.

[7] C. Gosselin, R. Duballet, P. Roux, N. Gaudillière, J. Dirrenberger, P. Morel, Mater. Des. **2016**, *100*, 102.

[8] NSF Workshop on Additive Manufacturing for Civil Infrastructure Design and Construction, 2017, https://events.tti.tamu.edu/conference/nsf-3dp-workshop/

[9] Q. Zhang, X. Yang, P. Li, G. Huang, S. Feng, C. Shen, B. Han, X. Zhang, F. Jin, F. Xu, T.J. Lu, Prog. Mater. Sci. **2015**, *74*, 332.

[10] E. Munch, M.E. Launey, D.H. Alsem, E. Saiz, A.P. Tomsia, R.O. Ritchie, Sci. **2008**, *322*, 1516.

[11] L.J. Gibson, M. F. Ashby. *Cellular solids: structure and properties*, Cambridge university press, **1999**.

[12] S. W. Cranford, A. Tarakanova, N.M. Pugno, M.J. Buehler, Nat. **2012**, *482*, 72.

[13] Y. Zhang, H. Yao, C. Ortiz, J. Xu, M. Dao, J. Mech. Behav. Biomed. Mater. **2012**, *15*, 70.

[14] E. Lin, Y. Li, J.C. Weaver, C. Ortiz, M.C. Boyce, J. of Mater. Res. **2014**, *29*, 1867.

[15] H. Ming-Yuan, J.W. Hutchinson, Int. J. Solids Struct. **1989**, *25*, 1053.

[16] M.Y. He, A.G. Evans, J.W. Hutchinson, Int. J. Solids Struct. **1994**, *31*, 3443.

[17] G. Noselli, V.S. Deshpande, N.A. Fleck, Int. J. Fract. **2013**, *183*, 241.

[18] C. L. Salinas, E. E. de Obaldia, C. Jeong, J. Hernandez, P. Zavattieri, D. Kisailus, J. Mech. Behav. Biomed. Mater. **2017**, 76, 58.

[19] E. E. de Obaldia, C. Jeong, L.K. Grunenfelderb, D. Kisailus, P. Zavattieri, J. Mech. Behav. Biomed. Mater. **2015**, 48, 70.

[20] J. J. Biernacki, J. W. Bullard, G. Sant, K. Brown, F.P. Glasser, S. Jones, T. Ley, R. Livingston, L. Nicoleau, J. Olek, F. Sanchez, J. Am. Ceram. Soc. **2017**, *100*, 2746.

[21] W. Gao, Y. Zhang, D. Ramanujan, K. Ramani, Y. Chen, C.B. Williams, C.C. Wang, Y.C. Shin, S. Zhang, P.D. Zavattieri, Comput. Aided Des. **2015**., *69*, 65.

[22] B. Zareiyan, B. Khoshnevis, Automat. Constr. **2017**, 81, 112.

[23] G. Franchin, P. Scanferla, L. Zeffiro, H. Elsayed, A. Baliello, G. Giacomello, M. Pasetto, P. Colombo, J. of Eur. Ceram. Soc. **2017**, *37*, 2481.

[24] A. Perrot, D. Rangeard, A. Pierre, Mater. Struct. **2016**, *49*, 1213.

[25] P. Shakor, J. Sanjayan, A. Nazari, S. Nejadi, Constr. Build. Mater. **2017**,*138*, 398.

[26] B. Zareiyan, B. Khoshnevis, Automat. Constr. **2017**, 83, 212.

[27] B. Panda, S. C. Paul, M. J. Tan, Matter. Lett. **2017**, 209, 146.

[28] S. C. Paul, Y.W. D. Tay, B. Panda, M. J. Tan, Arch. Civ. Mech. Eng. **2018**, 18, 311.

[29] T. T. Le, S. A. Austin, S. Lim, R. A. Buswell, R. Law, A. GF. Gibb, T. Thorpe, Cement. Concrete. Res. **2012**, 42, 558.

[30] P. Shakor, J. Sanjayan, A. Nazari, S. Nejadi, Constr. Build. Mater. **2017**, 138, 398.

[31] D. D. Higgins, J. E. Bailey, J. Mater. Sci. **1976**, *11*,1995.

[32] N. B. Eden, J. E. Bailey, J. Mater. Sci. **1984**, *19*, 150.

[33] L. J. Struble, P.E. Stutzman, E.R. Fuller, J. Am. Ceram. Soc., **1989**, *72*, 2295.

[34] M. Hambach, D. Volkmer, Cem. Concr. Compos. **2017**, *79*, 62.

[35] P. Feng, X. Meng, J.F. Chen, L. Ye, Constr. Build. Mater. **2015**, *93*, 486.

[36] L. J. Struble, P.E. Stutzman, E.R. Fuller, J. Am. Ceram. Soc., **1989**, *72*, 2295.

[37] Harsh, S., Shen, Z. and Darwin, D., 1990. Strain-Rate Sensitive Behavior of Cement Paste and Mortar in Compression.

[38] V.C. Li, M. Maalej, Y-M. Lim, in *Fracture of Brittle Disordered Materials: Concrete, Rock and Ceramics* (Eds: G. Baker, B. L. Karihaloo), CRC Press. **2004**, Part 2.

[39] J.C. Weaver, G.W. Milliron, A. Miserez, K. Evans-Lutterodt, S. Herrera, I. Gallana, W.J. Mershon, B. Swanson, P. Zavattieri, E. DiMasi, D. Kisailus, **2012**. Sci. *336*, 1275.

[40] Suksangpanya, N., Doctoral Thesis, Purdue University, December, **2016**.

[41] N. Suksangpanya, N. A. Yaraghi, D. Kisailus, P. Zavattieri, J. Mech. Behav. Biomed. Mater. **2017**, 76, 38.

[42] N. Suksangpanya, N. A. Yaraghi, R. B. Pipes, D. Kisailus, P. Zavattieri, Int. J. Solids Structs. **2018**, in review.

[43] Chen, X., Wu, S. and Zhou, J., Constr. Build. Mater. **2013**, *40*, 869.

[44] ASTM C150 – 17, Standard Specification for Portland Cement.

[45] ASTM C494 – 16, Standard Specification for Chemical Admixtures for Concrete.

[46] M. Moini, *Master's thesis*, University of Wisconsin-Milwaukee, August, **2015**.

[47] ASTM C1161 – 13, Standard Test Method for Flexural Strength of Advanced Ceramics at Ambient Temperature.

[48] A. Börger, P. Supancic, R. Danzer, J. of Eur. Ceram. Soc. **2002**, *22*, 1425.

[49] A. Börger, P. Supancic, R. Danzer, J. of Eur. Ceram. Soc. **2004**, *24*, 2917.

[50] Y. Cao, P. Zavaterri, J. Youngblood, R. Moon, J. Weiss, Cem. Concr. Compos. **2015**, *56*, 73.

[51] J.S. Magdeski, J. Univ. Chem. Technol. Metall. **2010**. *45*, 143.

[52] L.F. Nielsen, J. Am. Ceram. Soc. **1990**, *73*, 2684.

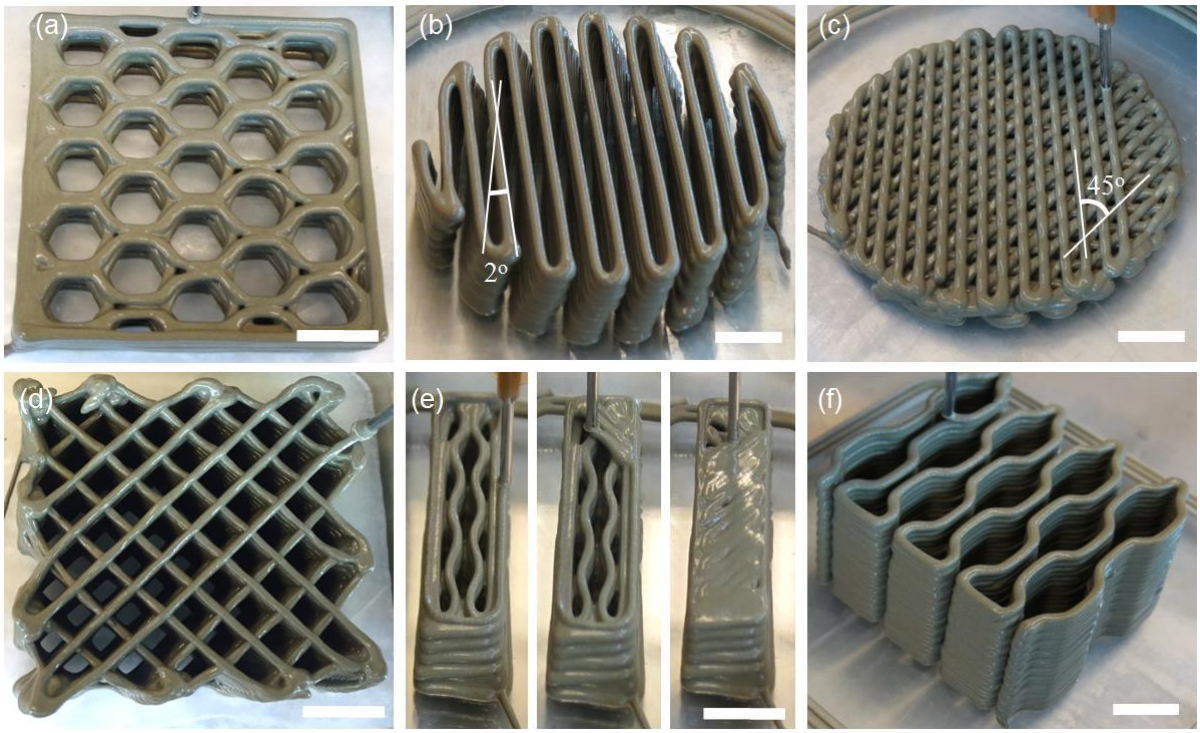

Figure 1. Various 3D printed architectures of hardened cement paste (hcp) elements: a) Closed cell honeycomb architecture; b-c) Bouligand architecture with, respectively, pitch angle $\gamma = 2^{o}$ and 45^{o}; d) Grid structure; e) Closed face sandwich panel beams with two solid layers at the top and bottom. f) Compliant structure with honeycomb architecture. All scale bars are 10.0 mm.

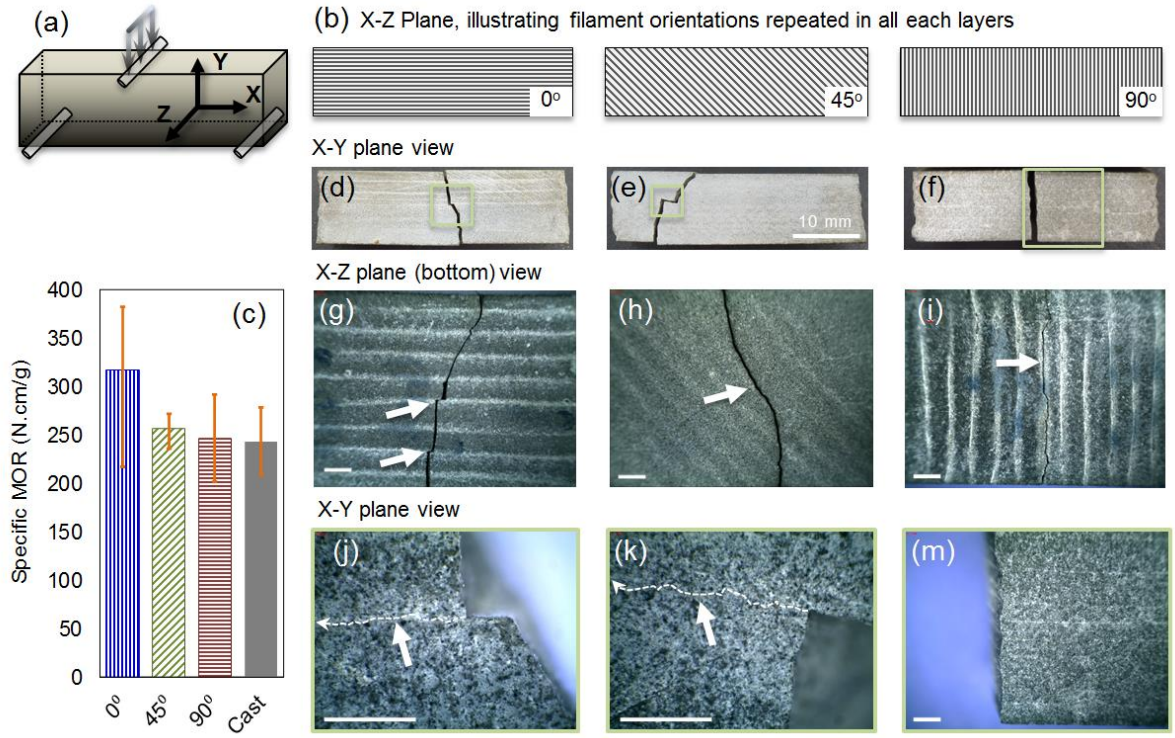

Figure 2. Mechanical response of 3D printed solid prisms with various architectures tested in 3PB: a) Schematic of the 3PB test illustrating orientation of the X,Y,Z axes b) Schematic of architectures plane view with orientation of the filaments repeated in all layers in X-Y c) Specific modulus of rupture of 3D printed elements with 0°, 45°, and 90° filament orientation versus cast specimens, d-i) Images of 0°, 45° and 90° specimens after failure illustrating crack patterns in X-Y plane view, g-i) X-Z plane (bottom) view, and j-m) micro-cracks in X-Y plane view in 0°, 45° prisms. All scale bars are 1.50 mm unless indicated.

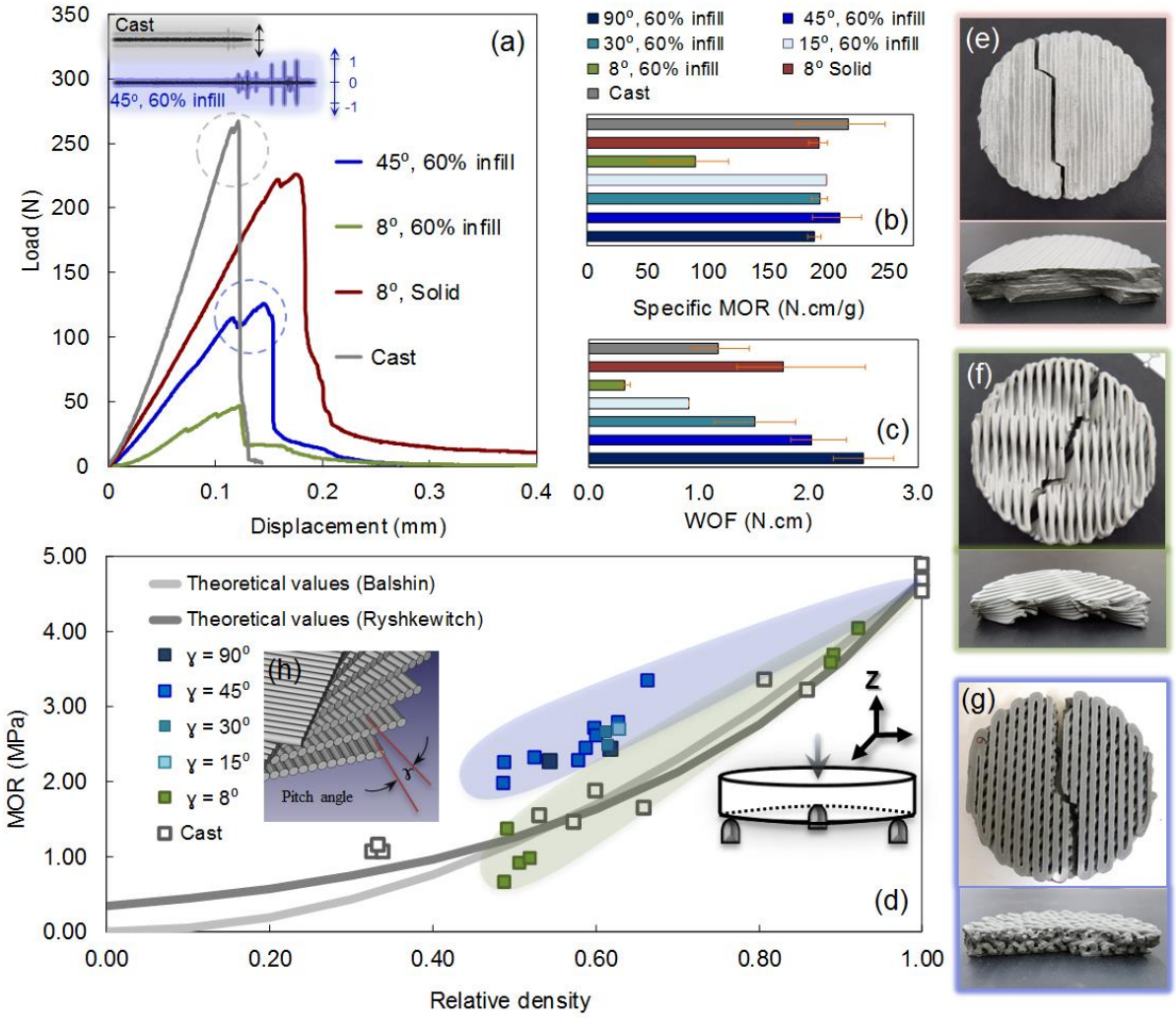

Figure 3. Mechanical response of Bouligand architecture using Ball-on-three-balls test. a) Load-displacement for printed disc specimens versus conventional cast controls, including screen shot of acoustic recording during testing. b) Specific modulus of rupture, c) Work of fracture, and d) Modulus of rupture versus relative density for Bouligand architectures with varying pitch angle ($\gamma = 8^o, 15^o, 30^o, 45^o, 90^o$) and percentage of infill (60% and 100%) compared to cast control discs, printed Bouligand architectures with e) $\gamma = 8^o$ with 100% infill f) $\gamma = 8^o$ with 60 % infill g) $\gamma = 45^o$ with 100% infill.

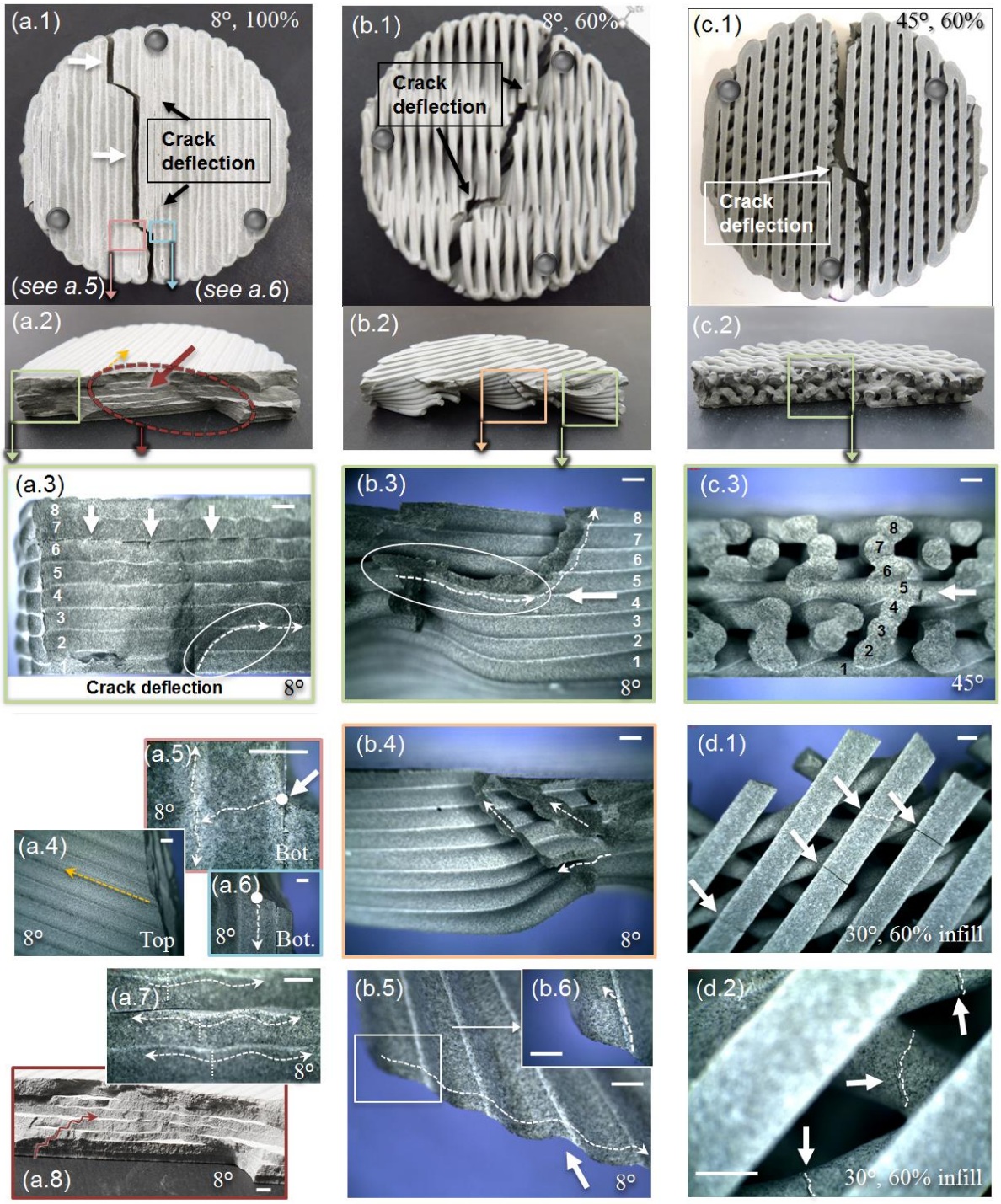
(a.1)
8°, 100%
Crack deflection
(see a.5)
(see a.6)
(b.1)
8°, 60%
Crack deflection
(c.1)
45°, 60%
Crack deflection
(a.2)
(b.2)
(c.2)
(a.3)
Crack deflection
8°
(b.3)
8°
(c.3)
45°
(a.5)
8°
Bot.
(a.4)
8°
Top
(a.6)
8°
Bot.
(b.4)
8°
(d.1)
30°, 60% infill
(a.7)
8°
(a.8)
8°
(b.5)
(b.6)
8°
(d.2)
30°, 60% infill

Figure 4. Crack paths and fracture patterns of various 3D printed Bouligand architectures: a1-a8) γ = 8^{o}, 100% infill, b1-b6) γ = 8^{o}, 60% infill, c1-c3) γ = 45^{o}, 60% infill, and d1,d2) γ = 30^{o}, 60% infill after B3B test. All scale bars are 1.0 mm.

Supporting Information

Additive Manufacturing and Performance of Architectured Cement-based Materials

*Mohamadreza Moini, Jan Olek, Jeffrey Youngblood, Bryan Magee, Pablo D. Zavattieri**

A honeycomb architecture with close cell (**Figure S1**a) and open cell (compliant) design (**Figure S1**b) is demonstrated. The compliant structure can demonstrate bilinear stress-strain behavior, including a primary linear strain recovery (*E1*) at strains below which the layered filaments make contact (cycles 1-5 in **Figure S1**c1) and a secondary linear response above strains (*E2*) at which the filament's contact take place (cycles 6 in **Figure S1**c1). As can be seen, the jointless compliant structure shown, exhibits two discrete moduli (*E1, E2*) depending on whether the filaments have made contact (**Figure S1**d,e) or not (**Figure S1**f,g). In contrast, the closed cell honeycomb architecture (HC) and cast element exhibit only one value of modulus (**Figure S1**c2). This dual response can be customized as applicable with suitable design of the architecture, spacing between filaments, and material property. The cast element represents a strain at failure of about 0.008. This is in the general range reported for typical hardened cement paste [31]. In complaint structure, in addition to the bi-linear response, a strain (as high as 0.025 in the bi-linear region) much higher than the strain at failure commonly observed for cast hardened cement paste (0.005 to 0.008) [31] is exhibited.

Video 1-4: Bouligand architecture with 15°, 30°, 45°, 90° pitch angle

Video 5,6: Two typical compliant structure

Video 7-9: Sandwich panel beams with closed top and bottom face

Video 10: Grid structure

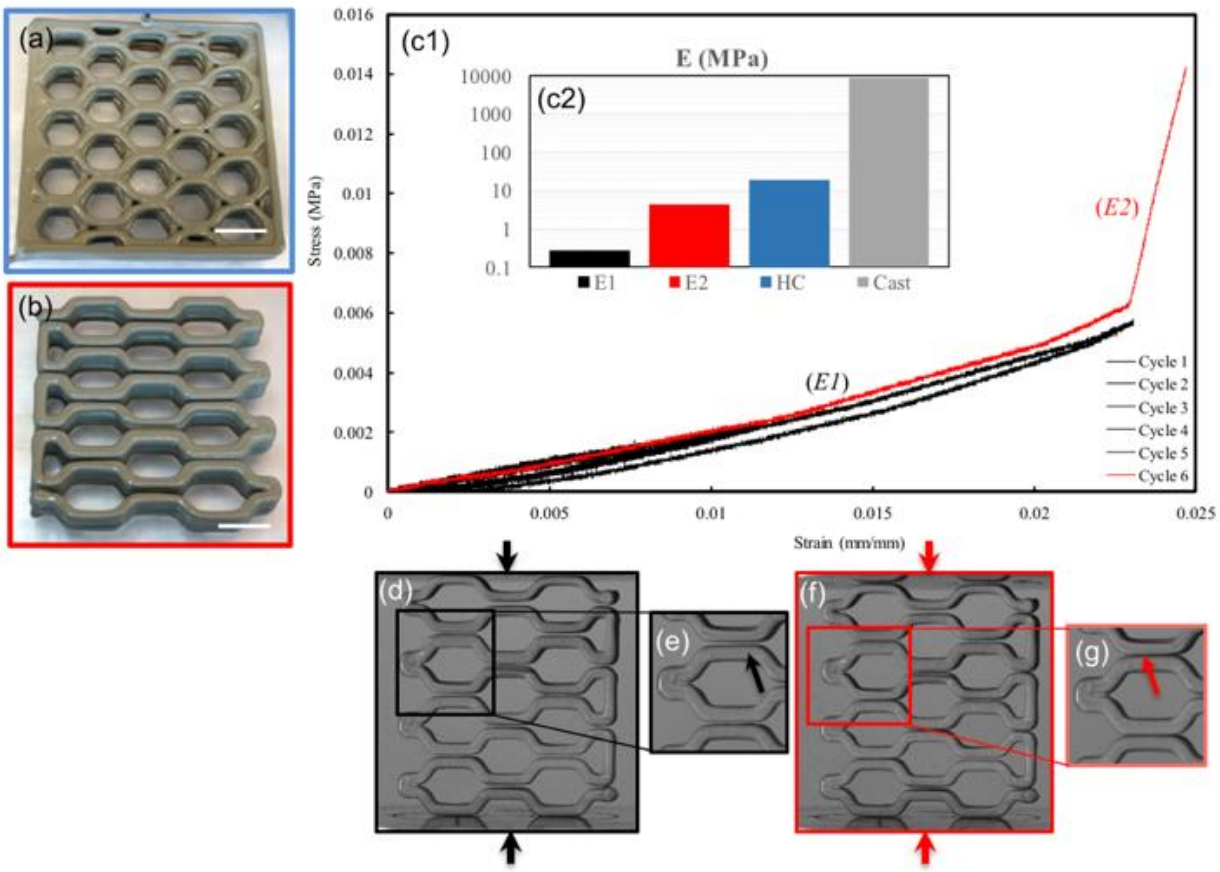

Figure S1. a) Closed cell honeycomb structure. b) Compliant structure with honeycomb architecture. c) Bilinear stress-strain behavior including five primary linear strain recovery (Cycles 1-5) and secondary response (Cycle 6) before and after filament's contact. c-i) Comparison of two discrete moduli of elasticity of compliant structure (*E1*,*E2*) with closed cell honeycomb and cast. d,e) Compliant structure in cyclic loading (cycles 1-5) prior to filament's contact. f,g) Compliant structure after filament's contact takes place.

Click here to access/download
Supporting Information
Vid 1. Bouligand, 15 Deg..mp4

Click here to access/download
Supporting Information
Vid 2. Bouligand, 30 Deg..mp4

Click here to access/download
Supporting Information
Vid 3. Bouligand, 45 Deg..mp4

Click here to access/download
Supporting Information
Vid 4. Bouligand, 90 Deg..mp4

Click here to access/download
Supporting Information
Vid 5. Compliant Structure 1.mp4

Click here to access/download
Supporting Information
Vid 6. Compliant Structure 2.mp4

Click here to access/download
Supporting Information
Vid 7. Sandwich Panel 1.mp4

Click here to access/download
Supporting Information
Vid 8. Sandwich Panel 2.mp4

Click here to access/download
Supporting Information
Vid 9. Sandwich Panel 3.mp4

Click here to access/download
Supporting Information
Vid 10. Grid Structure.mp4